Contaminant Ultrasonic Removal via Vibration Ejection from Solar cells

Technical Paper and Verification Demonstration Results

Brenden Anich[1]
Zachary Boeringa[1]
Logan Feld[1]
Andrew Koenig[2]
Zoe Reed[3]
Jeremiah Rittenhouse[4]
Caitlin Thomasson[3]
Lauren Tomanek[5]
Elizabeth Trn[1]

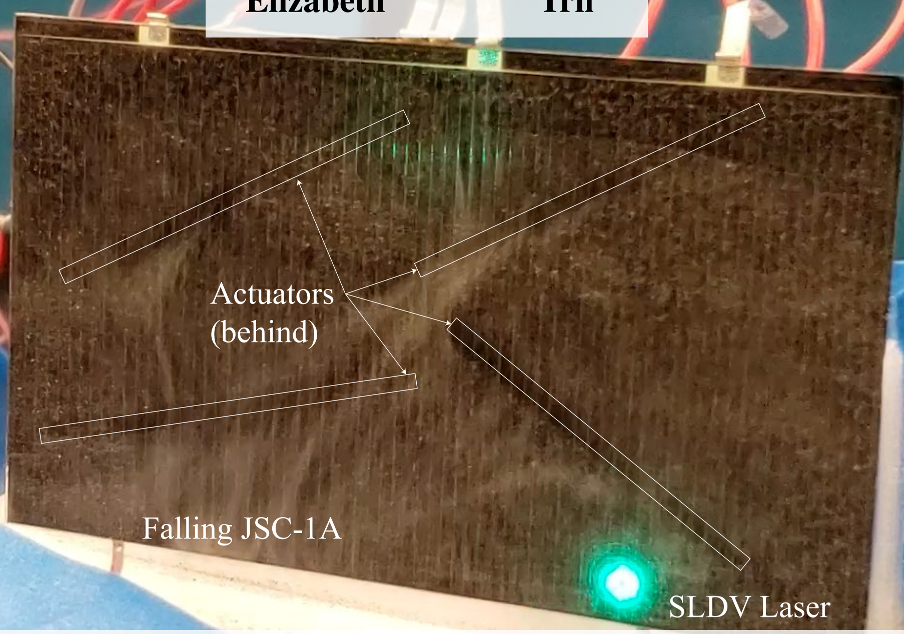

MISSOURI UNIVERSITY OF SCIENCE AND TECHNOLOGY

Space Grant Affiliation: Missouri University of Science and Technology
Space Grant director: Dr. K.M. Isaac, (573)-341-4604, isaac@mst.edu

[1]Undergraduate, Aerospace Engineering
[2]Undergraduate, Mechanical Engineering
[3]Undergraduate, Ceramic Engineering
[4]Graduate, Aerospace Engineering
[5]Graduate, Mechanical Engineering

Advised by:

Daniel S.	Stutts	Missouri University of Science and Technology
Yezad H.	Anklesaria	Missouri University of Science and Technology
Jonathan	Kimball	Missouri University of Science and Technology
Fatih	Dogan	Missouri University of Science and Technology
Daoru	Han	Missouri University of Science and Technology
Ed	Kinzel	University of Notre Dame
Leslie S.	Gertsch	Missouri University of Science and Technology

October, 2021. Falling JSC-1A lunar regolith simulant captured an instant after high-power actuation of the Rotated PZT prototype. Prototype designed August, 2021, using Lauren Tomanek's ANSYS multiphysics surface acceleration optimization script.

Contents

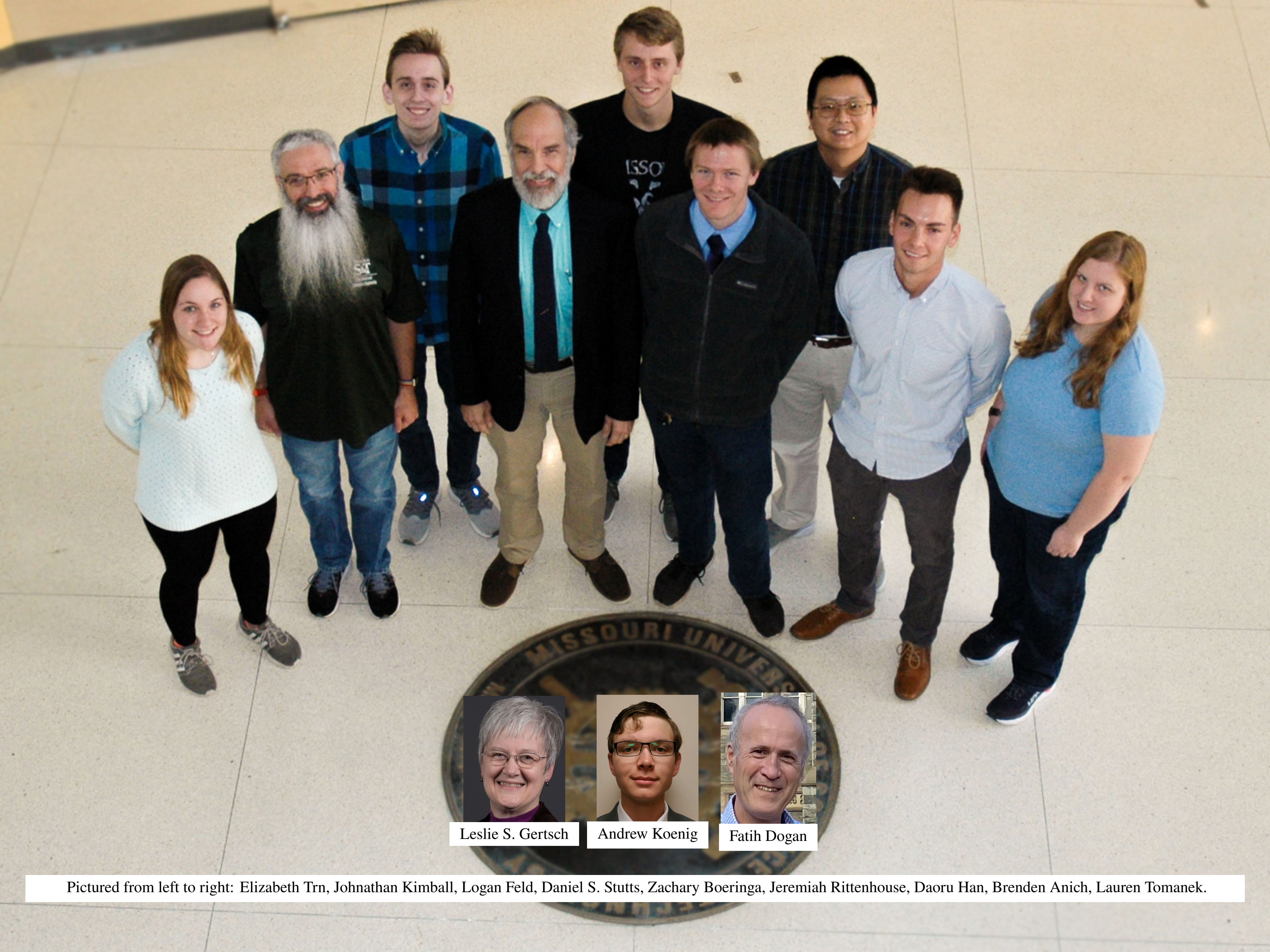

Pictured from left to right: Elizabeth Trn, Johnathan Kimball, Logan Feld, Daniel S. Stutts, Zachary Boeringa, Jeremiah Rittenhouse, Daoru Han, Brenden Anich, Lauren Tomanek.

Missouri University of Science and Technology: Contaminant Ultrasonic Removal via Vibration Ejection from Solar cells

Concept Synopsis

- Lunar dust tends to adhere to any surface available.
- When dust adheres to solar cells it reduces the solar cell's ability to generate power.
- The proposed solution is to use piezoelectric actuators to induce large accelerations on the solar cell's surface sufficient to overcome Van der Waal's forces that adhere lunar dust to solid objects.
- CURVES mitigates dust by periodically removing adhered dust using piezoelectric actuators to excite structural modes.

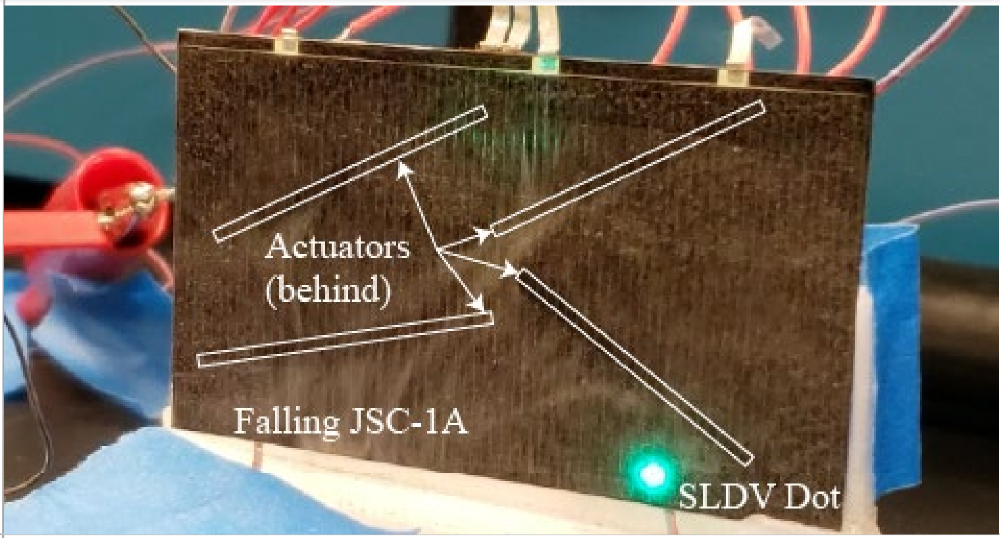

Innovations

- CURVES use of piezoelectric actuation extends the capabilities of surface dust mitigation without damaging any components themselves.
- Optimization of the piezoelectric actuator location increases average surface acceleration.
- Refinement of the driving frequency during testing improves efficiency to minimize required power usage.
- ITO coated glass improved dust removal efficacy.
- By removing human intervention, CURVES extends possible mission duration for both static and vehicular missions, and eases power worries for long-term manned missions.

Verification Testing Results & Conclusions

- In a single three second cycle, CURVES reclaims an average of 49% of lost power due to accumulated dust when actuated under Earth conditions.
- CURVES survived cryogenic thermal cycling without any sign of degradation.
- Novel phase-locked-loop method resonance tracking circuit produced preliminary glass slide dust removal results at low-power ~1.2 [W] as effective as untracked, high-power ~60 [W] testing.
- CURVES controlling circuit can track the resonance frequency to maintain peak efficiency.
- Predicted returned energy per mass of CURVES is 154 $\left[\frac{MJ}{kg}\right]$ over the course of a single year.

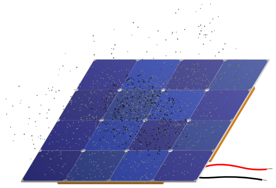

Brenden Anich
Zachary Boeringa
Logan Feld
Andrew Koenig
Zoe Reed
Jeremiah Rittenhouse
Lauren Tomanek
Caitlin Thomasson
Elizabeth Trn

1 Executive Summary

The project **"Contaminant Ultrasonic Removal via Vibration Ejection from Solar cells"** (CURVES) aims to mitigate dust accumulation on lunar photovoltaic arrays by bonding a system of piezoelectric Lead Zirconate Titanate (PZT) actuators to the inactive side of solar cells in ground-based or vehicle-based arrays. Once deployed, the actuators can be electrically driven on occasion to induce surface vibrations, producing surface acceleration on the solar cell sufficient to overcome contaminant adhesive forces.

Contaminant buildup on solar arrays leads to reflective loss, decline in efficiency, and reduced power generation. Lunar dust is particularly adhesive, with estimated cohesion force from 0.01 to 0.1 [kPa] [1]. Even the astronauts in the first landings on the lunar surface noted its tendency to stick to any and all contact surfaces [2]. Previous work by Dr.Yezad Anklesaria shows piezoelectric actuators' ability to shake a variety contaminants from quartz-crystal glass. CURVES aims to do the same: shaking lunar dust off of solar cells.

Primary testing, with the purpose of verifying Finite Element Analyses used to design CURVES, was performed in a laboratory environment. Efficacy and efficiency are determined by testing with a light coating of dust, as may be expected in the lunar environment, gauged by I-V curve testing to find the reclaimed generation ability of the solar cells. Environment testing was performed in a cryogenic vacuum chamber at relevant conditions of 170 [K] and 1.7×10^{-6} [Torr].

Technology to clean solar panels, camera lenses, and exterior view windows without relying on unknown natural methods or the necessity for astronaut maintenance improves the longevity and viability of future long-term lunar missions . Implementing self-cleaning solar cells especially improves viability of remote instruments and facilities with inconsistent human presence, increases survivability if extra-vehicular activity (EVA) becomes impossible, and reduces reliance on nuclear power. An emphasis on high-longevity technology opens up possibilities of permanent human presence on extra-terrestrial bodies. CURVES provides a base system design which can be easily modified to meet requirements in deployment, allowing for a cleaner, low-maintenance power supply for lunar missions and other applications.

Recent efforts to address the contaminant removal problem through the use of harmonically excited structural modes show significant promise. Contaminant ejection forces are proportional to surface acceleration, and therefore to the square of the driving frequency [3, 4]. The ability to drive vibrations at high frequencies and tracking optimal vibration frequencies, allows CURVES to achieve maximum clearance, with atmospheric testing showing the system currently capable of restoring in a single drive cycle as much as 80 [%] of power generation lost to surface fouling. Substrates are driven in the ultrasonic frequency range by attached piezoelectric elements with the determined frequency range depending on the size and shape of the substrate, and on the modes desired.

2 Problem Statement and Background

Reduced thermal efficiencies from insulation, mechanical failures from abrasion or gumming, abrasive seal failures in space suits, and inhalation hazards within habitat areas from dust contamination all pose major threats to the long-term viability and safety of lunar missions [5]. Surface contamination of solar cells has not yet greatly affected lunar missions in particular, but carries significant impact for Martian missions already. The 2018 loss of communication with the Mars *Opportunity* rover to surface fouling following a dust storm highlights the consequences of such coverage [6]. With greater traffic and mission endurance associated with a permanent base on the moon, surface fouling issues are certain to crop up. Dust carries little potential for long-term harm to solar cells by abrasion or impact, but cells being rendered ineffective by surface fouling is a significant danger.

Solar wind lofting, rocket launches and landings, and meteorite impacts, all loft large amounts of dust into the space immediately above the surface of the moon, creating a haze at the surface [5]. The scale of the projects required render prevention of lofting by solar winds and meteorites impractical, therefore dust removal seems the most efficient method of dust mitigation, requiring smaller amounts of power for shorter periods than attempting a constant dust shield.

The method of removal is highly significant. Under normal conditions, dust does not generally have enough momentum to seriously damage solar cells by impact and is not likely to cause significant abrasion damage on stationary solar cells. A method of dust removal must be carefully chosen to not introduce either of these dangers. Multiple such methods do exist, methods that require no direct mechanical interaction with dust contaminants, including Electrostatic Dust Shielding (EDS), fluid-based dust removal, and high-acceleration surface vibrations.

In lunar environments, fluids are impractical due to the required mass, limited usage, and potential to introduce abrasion from the blown or flowing dust. Furthermore, most fluids do not maintain their desired properties when exposed to high vacuum, tending to rapidly boil and disperse. EDS systems can be power-hungry and require high voltages, though are relatively low-mass and can eject dust in a controlled direction.

Vibration dust mitigation was chosen for its relatively low-mass characteristics, ability to remove fine particles, and lower power and voltage requirements. Several common methods to induce vibrations into a body present themselves. Spinning an imbalanced load can introduce vibrations, but mass requirements and the tendency of lunar dust to gum up and destroy moving mechanisms prevents this [5]. Devices that produce acoustic vibrations commonly use one of two types of actuators. Large-scale speakers use wire-coil actuators to produce high-authority vibrations with permanent magnets within looped coils. Smaller-scale speakers, such as those found in smart phones, utilize piezoelectric ceramics to produce vibrations.

Piezoelectrics provide an excellent solution to the dust mitigation problem. PZT actuation requires no moving parts and is easy to integrate onto the solar cells themselves. Ceramic piezoelectrics provide a further benefit in that the piezoelectric effect is reversible. The actuators themselves provide an intrinsic method of detecting the phase difference between controller signal and the vibration phase of the solar cells themselves (see Section 3.4), enabling in-operation optimization of vibration frequency for optimal efficacy and efficiency.

The difficulty with creating a system of piezoelectric actuators to mitigate dust lies in the optimization of the system to achieve maximum efficacy with minimal power requirements. A controller and powering system must also be created that is capable of delivering the necessary voltage while detecting phase changes, which are a result from mass changes in the system and nonlinear actuation effects upon the PZT elements.

3 Project Description

3.1 Concept Lifecycle

3.1.1 Initial Idea

CURVES received its conception in the graduate work of Dr. Yezad Anklesaria, who used PZT actuators to create a more effective method of cleaning camera lenses. CURVES reapplies this technology and the method of development to produce a technology for dust mitigation in other applications in which the final location of the dust is fairly irrelevant, such as cleaning of exterior surface fouling. Exterior surface fouling causes a number of issues to a system, including decreasing the ability of solar cells to produce power. This loss of power may potentially reduce or destroy the capabilities of an entire mission.

PZT actuation is an ideal solution to this problem. Because PZT actuation requires no moving parts, it is invulnerable to dust abrasion, is light and simple to add, and can be easily controlled. PZT actuation also induces waves directly into the surface of the material it is attached to more efficiently than the common alternative of a spun imbalanced load. Furthermore, following installation, a PZT system requires only power to function, and can be turned on and off as needed, not requiring power outside times the system is active, nor requiring any other input resources.

3.2 Finite Element Analysis Optimization

ANSYS Finite Element Analysis optimization determined the best PZT placement to achieve dust mitigation. Using model simulation reduced prototype revisions and developed an understanding of the influence of actuator placement and dimensions on prototype performance.

Maximizing the average normal surface acceleration on the solar cell force while also optimizing other factors required an adaptive multiple-objective method in ANSYS. These other requirements included ensuring the prototype survived actuation, minimizing dynamic tensile and compressive stresses in the PZT elements, and minimizing von Mises equivalent stress in the solar cell. The robustness of this method and its openness in not needing a predetermined design topology contributed to its selection.

3.2.1 Modeling

Setup of the optimizations included modeling the geometry of the actuators as 3D elements and the solar cell as a collection of surface elements in SpaceClaim, the geometry modeler within ANSYS. Surface elements were chosen due to the ratio between the thickness to the length and width allowed the application of plate theory. An example model is shown in Figure 3.1. Typically in FEA analysis the bond between objects is ignored; however, the bond becomes critical with PZT and cannot be neglected.

The Coupled Field Harmonic Analysis used to model the multi-physics problem used full piezoelectric, stiffness, and permittivity matrices, specifically those of PZT-4, the PZT formulation used throughout CURVES development. An epoxy layer model provided the normal stiffness contact factor that defines how much two bonded objects can move normally relative to each other for optimization routines. This also allows for the damping within the epoxy layer that physical prototypes clearly display.

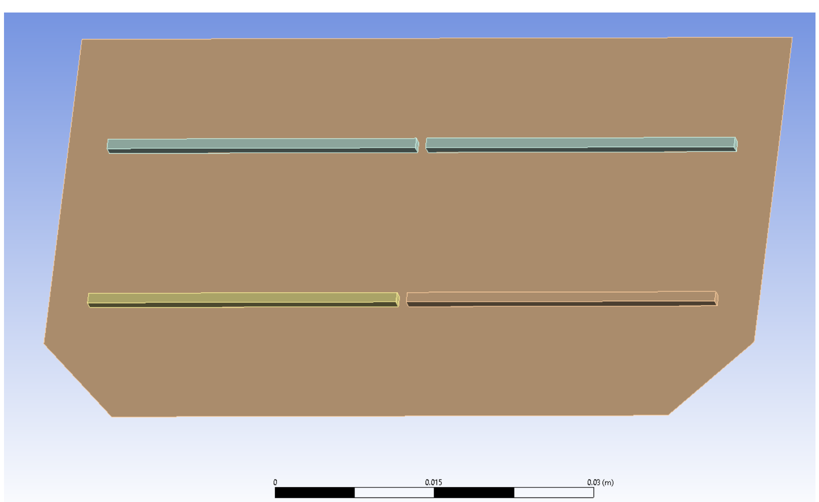

Figure 3.1. Model Setup in ANSYS

3.2.2 Meshing

Meshing the PZT elements using tetragonal elements aligned with the axis of polarization ensured appropriate application of voltage. The surface elements in the solar cell included the thickness of the solar cell. Figure 3.2 shows and example mesh. All elements used were a quadratic order to better characterize the response. The voltage was applied to the top face of the PZT elements and grounded to the face attached to the solar cell.

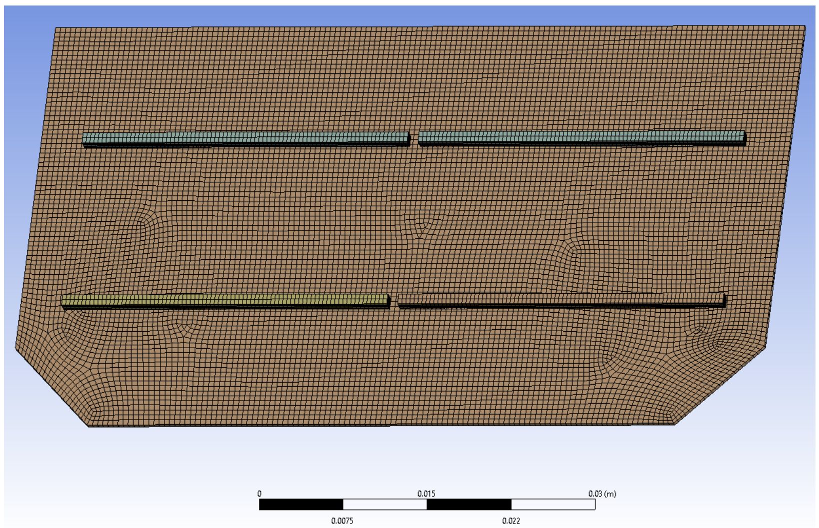

Figure 3.2. Mesh Setup in ANSYS

3.2.3 Harmonic Analysis

A two step-procedure yielded the optimum frequency of excitation, and thus the maximum acceleration. The custom harmonic analysis, created using an ANSYS APDEL code input, consisted of a coarse frequency sweep over the possible frequencies of interest–500 [kHz] to 2.5 [MHz]–in thirty steps, followed by a finer sweep around the optimal frequency found in the first sweep. The second sweep covered the span within one step of the first sweep, 133.4 [kHz], also in thirty steps, to achieve a 4.4 [kHz] resolution.

Design evaluations consisted of several parameters calculated after the second sweep, most importantly the maximum average acceleration on the solar cell surface. The nodes in the PZT are evaluated to find the maximum tensile and compressive stress in the normal direction. Last, the maximum von Mises equivalent stress is found in the solar cell nodes.

Additional parameter relationships added to the simulation to keep the PZT pieces on the solar cell and to prohibit the pieces from crossing each other ensured that the optimization routine would only try valid points. Also, in the phase optimization routine, one PZT was kept at fixed phase to provide a reference point.

3.3 Proposed Designs

ANSYS analysis produced three optimized designs: one with actuators oriented horizontal relative to the longest edge of the solar cell, one where the elements have an optimized pitch relative to the edges of the solar cells, and another with both optimized pitch and phase of excitation across the various PZT elements. For a control, a fourth non-optimized design, consisting of a square piece of PZT centered on the solar cell, was also created.

3.3.1 Horizontal Prototype

For this design, the vertical location of the PZT could move in addition to the length and width of the PZT. The harmonic analysis found the optimum frequency for each candidate design using the process outlined in Section 3.2.3. Figure 3.3 gives the dimensions of the optimized prototype and location of PZT elements. The prototype was optimized for the all four PZT to be electrically in-phase with each other as well as with actuators one and four out of phase with actuators two and three. Figures 3.4 and 3.5 show the normal acceleration results from ANSYS for in-phase and out-of-phase respectively.

3.3.2 Rotated Prototype

The rotated prototype extends the horizontal prototype optimization by adding an additional degree of rotation to each PZT element. Figure 3.6 gives the dimensions of the optimized prototype. Figures 3.7 and 3.8 show the resulting normal accelerations for both the in-phase and out-of-phase electrical configurations.

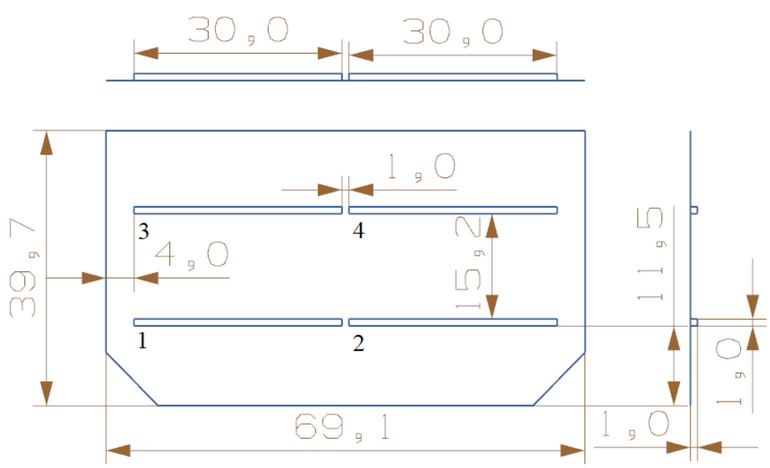

Figure 3.3. Horizontal Prototype Dimensions (mm)

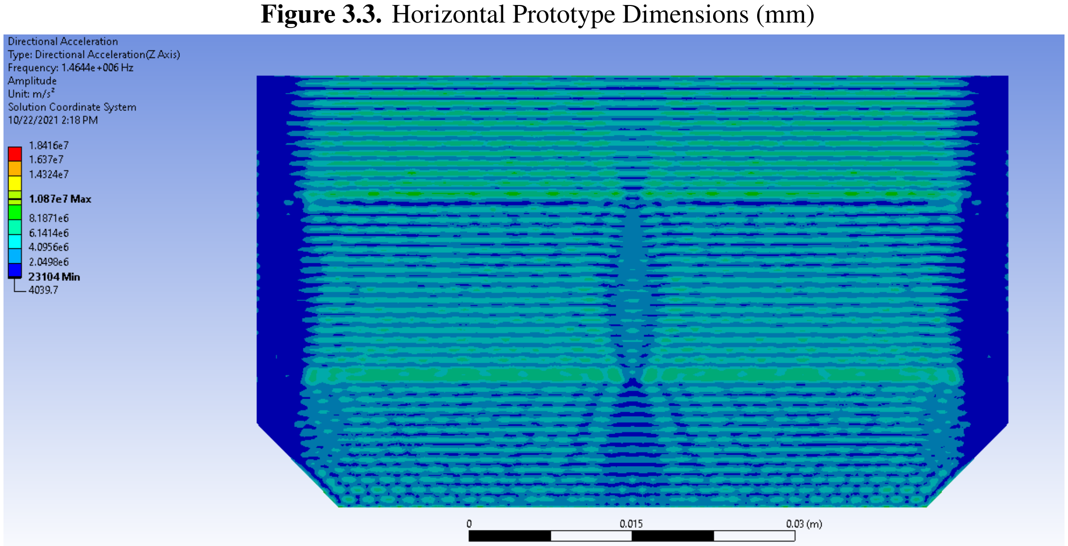

Figure 3.4. Horizontal Prototype In-Phase Normal Acceleration Amplitude

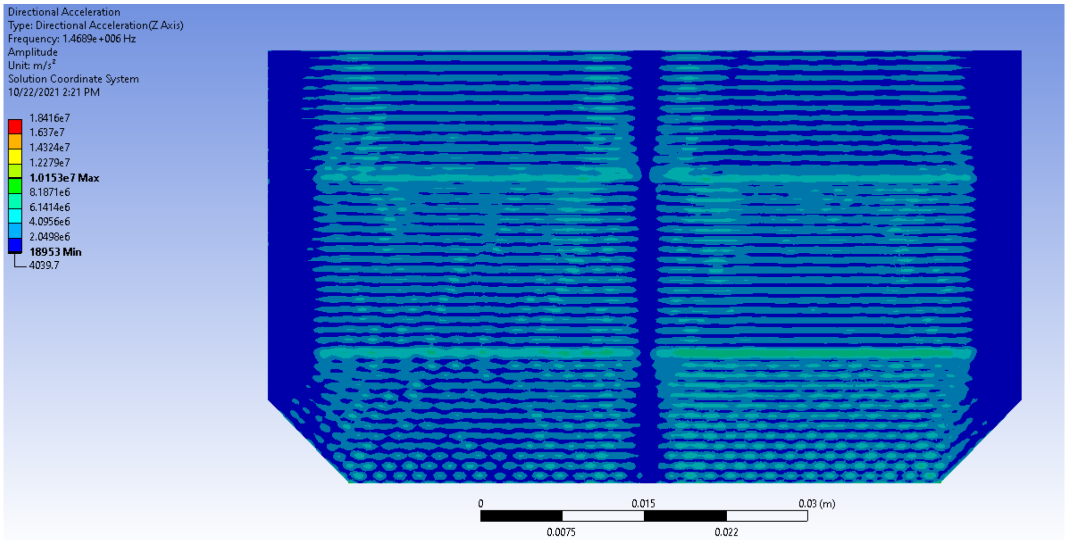

Figure 3.5. Horizontal Prototype Out-of-Phase Normal Acceleration Amplitude

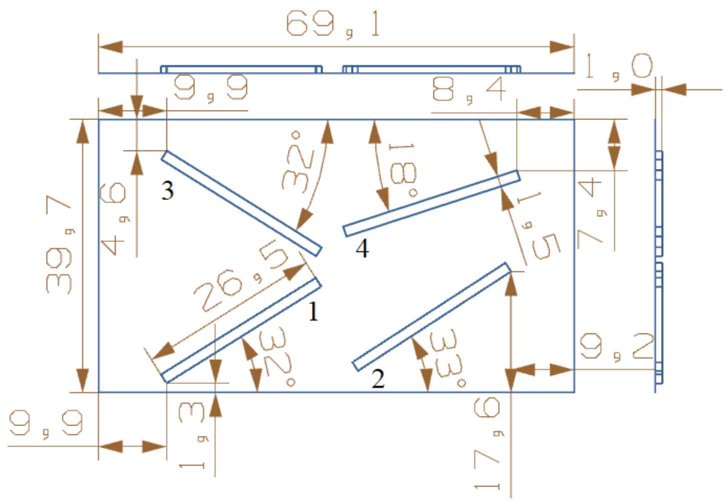

Figure 3.6. Rotated Prototype Dimensions (mm)

3.3.3 Phase Prototype

The phase prototype extends the rotated prototype into allowing the electrical phase of each PZT to vary as indicated in Table 3.1. Figure 3.9 gives the optimized phase prototype dimensions. Figure 3.10 shows the resulting normal acceleration.

3.3.4 Square Prototype

The only factor that is optimized in this design is the resonant frequency. The dimensions of the square piece of PZT were chosen such that the average area would be similar to the three optimized designs. A 11.5 [mm] square piece of PZT that was 1 [mm] thick was placed in the middle of the solar cell. The resulting maximum normal acceleration is shown in Figure 3.11. The maximum acceleration was $7.66x10^6 \left[\frac{\mathrm{m}}{\mathrm{s}^2}\right]$. The square prototype had the least acceleration compared to any of the optimized prototypes. The worst performing optimized design, the horizontal orientation, attained 33 [%] more acceleration than

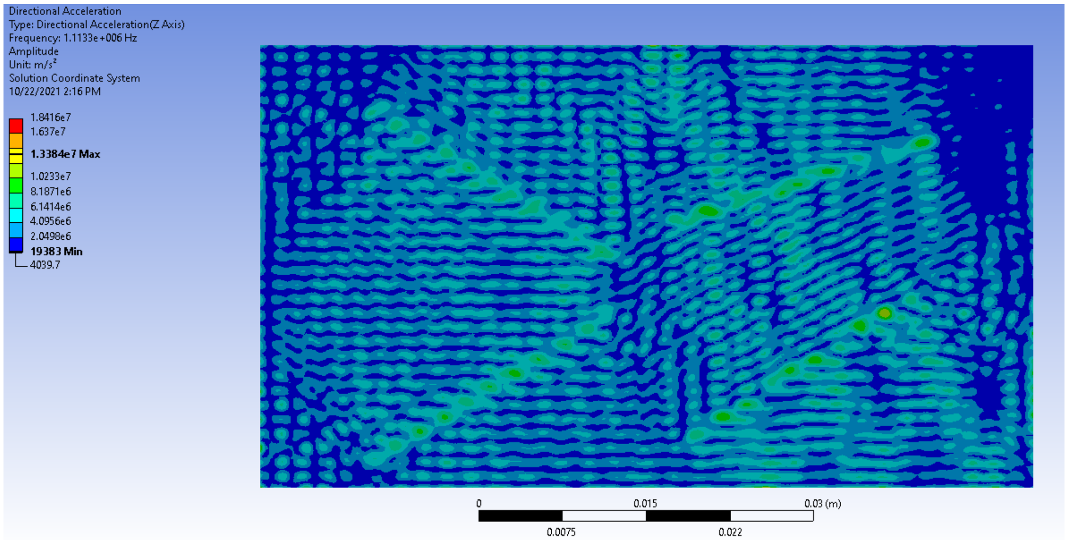

Figure 3.7. Rotated Prototype In-Phase Normal Acceleration Amplitude

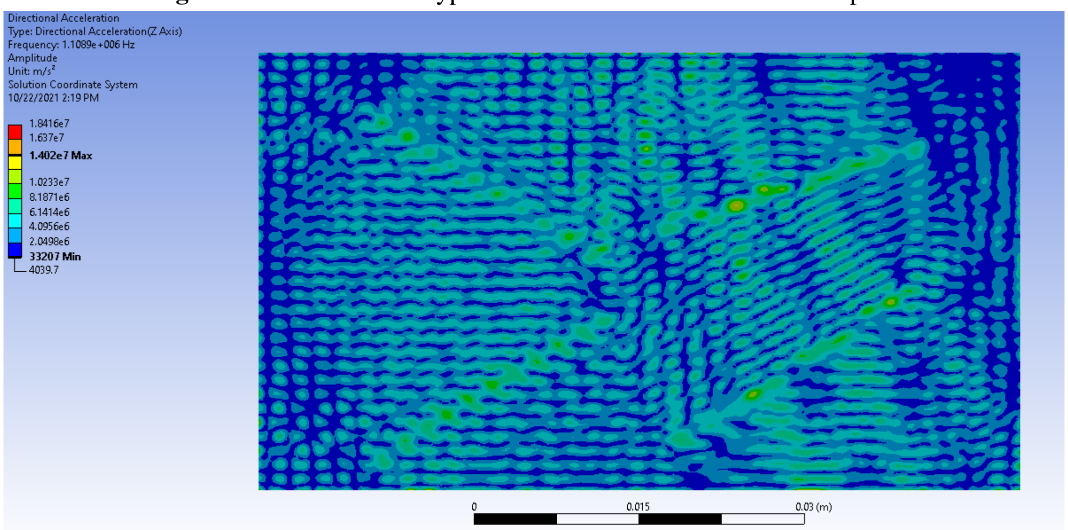

Figure 3.8. Rotated Prototype Out-of-Phase Normal Acceleration Amplitude

the square prototype, while the phase prototype garnered the largest maximum acceleration at 141 [%] more than the square prototype.

3.3.5 Prototype Summary

Table 3.2 gives a summary of the efficacy of the prototypes. The average acceleration was calculated using the nodes on the top surface of the solar cell. The acceleration was normalized using the procedure outlined in Section 4.3.1.

3.4 Circuit Design

Successfully implementing CURVES into real-world applications requires a circuit capable of tracking and amplifying the resonant frequency of a PZT actuator attached to a solar cell. Research shows that resonance in piezoelectrics occurs when voltage and current are in-phase. A thorough literature review

Table 3.1. Electrical Phase for Phase Prototype (mm)

PZT	Phase (Degrees)
1	0
2	324
3	301
4	230

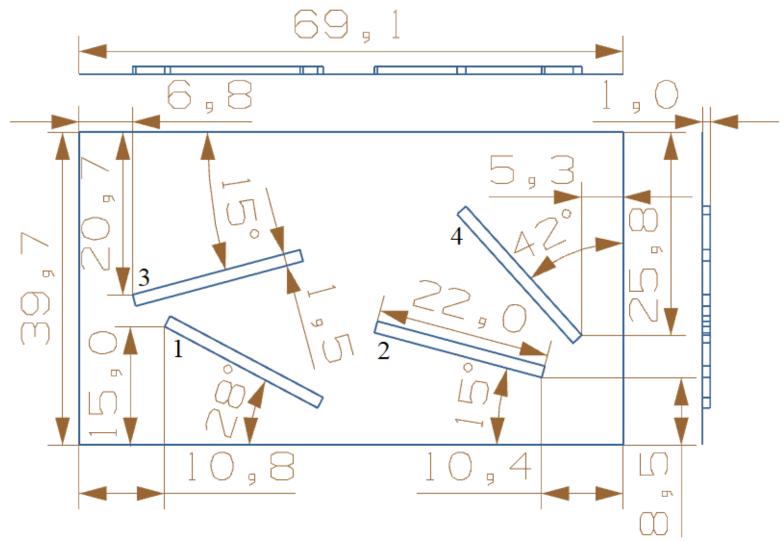

Figure 3.9. Phase Prototype Dimensions

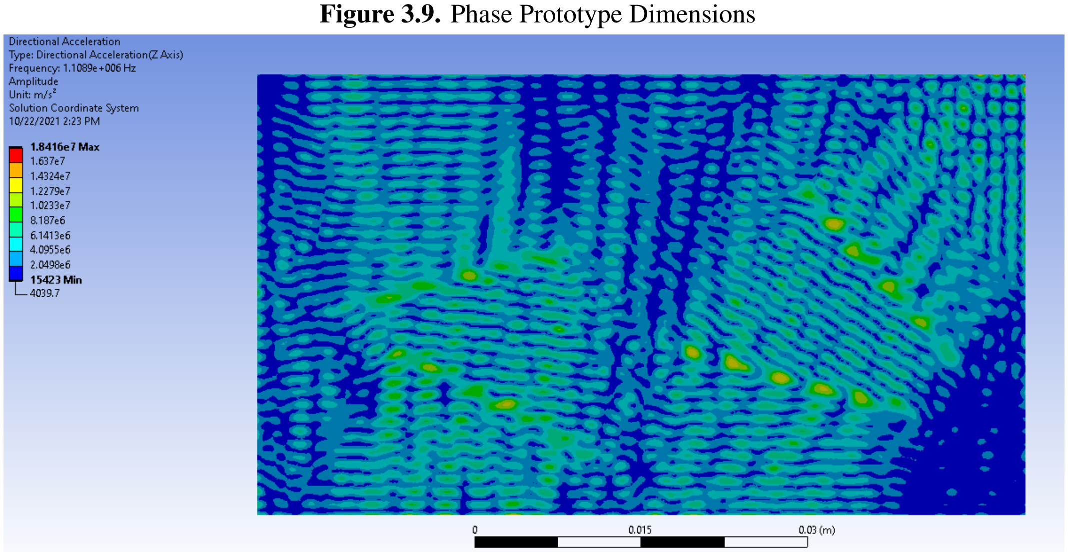

Figure 3.10. Phase Prototype Normal Acceleration Amplitude

revealed previous efforts to utilize a Phase Lock Loop (PLL) method to match the voltage and current phases. Thus PLL became the primary logic implemented in the circuit design and program.

The final circuit design for PZT actuation was developed in consultation with Dr. Jonathan Kimball. The design utilizes a Field Programmable Gate Array (FPGA) board known as XLR8 made by Alorium Technologies which can run custom VHDL code burned onto the board. The XLR8 board is a unique system in that it allows for the use of Arduino code to interact with the VHDL code as if it were a standard peripheral (called an Xcelerator Block or XB). The team developed an XB that tracks the resonance within the FPGA,

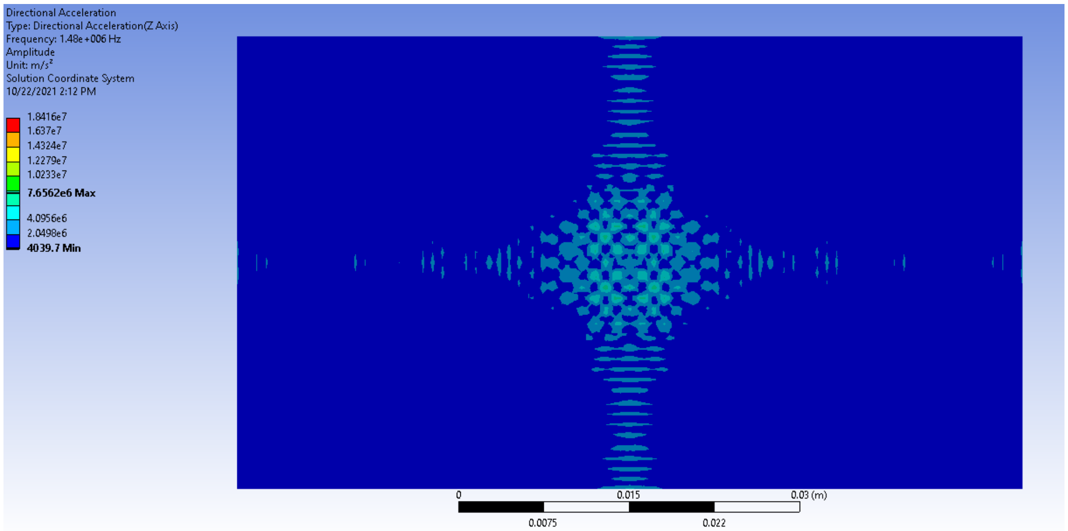

Figure 3.11. Square Prototype Normal Acceleration Amplitude

Table 3.2. ANSYS Prototype Summary

Prototype		Voltage [V]	Frequency [MHz]	Avg. Acc. $\left[\frac{m}{s^2}\right]$ x10^6	Normalized Acc. $\left[\frac{1}{Vs^2}\right]$ x10^3
Square		103	1.487	0.80	59.0
Horizontal	in-phase	85	1.464	3.81	373.4
	out-of-phase	55	1.469	2.52	381.5
Rotated	in-phase	78	1.113	3.04	244.8
	out-of-phase	87	1.109	3.36	242.6
Phase		103	1.109	3.48	229.6

configured by Arduino code. The XLR8 system utilizes a wrapping method that compiles the VHDL code, all the various programmed Arduino commands, and all registers addressed to each value sent to and received from the Arduino code, such that an Arduino interface can be created to interact directly with the VHDL PLL code to ensure the PZTs are actuating as intended. This interface also allows for significant control of how the PZT elements are actuating with the use of custom commands and peripherals. This board provides an Arduino interface to a power driver circuit that includes four switching legs, a boost converter circuit, and a polarity detection circuit that allows for the implementation of the PLL for resonance tracking of all four of the PZT elements present on a solar cell.

A custom-made polarity detection component (PCB1001 in Figure 3.12) ensures that the circuit runs at resonance by detecting the difference in frequency above or below resonance by the electrical impedance. Being above or below resonance creates a square wave that is then sent to the XLR8 board in combination with any inputs from the Arduino interface so the actual resonant frequency can be determined and set. This square wave output is denoted as Ipol.

Arduino served as the interface for the XLR8 XB. Inputs initializing a nominal, minimum, and maximum frequency, a duty cycle, and a PLL gain are sent to the VHDL program. The chosen nominal frequency is an approximate resonance frequency obtained from experimental data as described in Section 4.3.2.1. The minimum and maximum frequencies provide a range of frequencies where the exact resonance may occur.

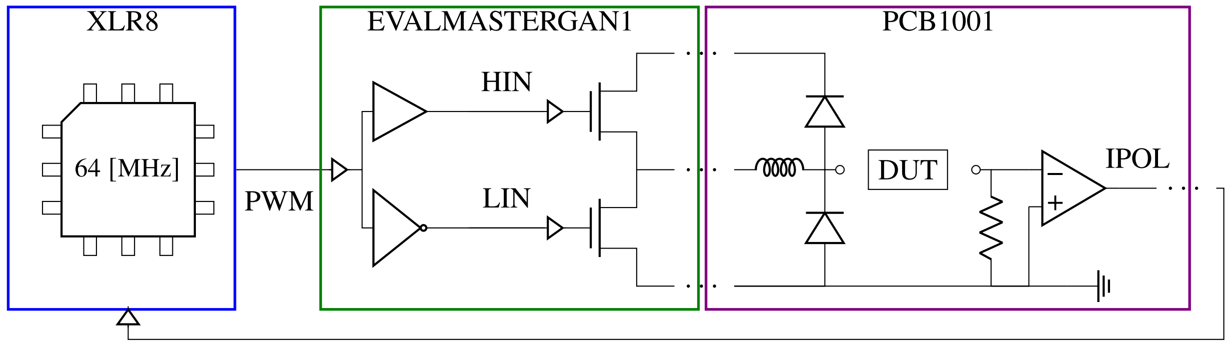

Figure 3.12. Drive Circuit Block Diagram

The interface also enables and disables the output and PLL integration, and toggles the phase of the four output signals individually.

The XLR8 FPGA board (XLR8 in Figure 3.12) implemented in the circuit runs code written in VHDL to be executed at a 64 [MHz] clock cycle for quick resonance determination. This VHDL code is also able to send to and receive information from the Arduino interface through on-board registers. The XLR8 reads in a nominal starting frequency, a minimum and maximum frequency to ensure the PLL tracks the desired resonant peak, a duty cycle, a value for the gain, the clock speed, and a control byte that contains various commands, all sent from the Arduino interface. This control byte contains information on whether each of the four PZTs should operate in-phase or out-of-phase, whether the signal should be buffered to run at a stored frequency value, whether the PLL should be enabled, and whether internal switching should be enabled. The VHDL code can then output eight signals, two for each PZT, that allow the individual PZTs to run in-phase or out-of-phase depending on how the control byte is programmed. The code also returns the actual resonant frequency determined by the PLL system to the Arduino interface and an internal signal that the VHDL code uses for resonance tracking, denoted Vpol.

The XLR8 outputs then go to an EVALMASTERGAN1 board (EVALMASTERGAN1 in Figure 3.12), which integrates a MASTERGAN1 from ST Microelectronics with some control and protection circuitry. This board and chip enables designers to quickly use GaN HEMTs without having to worry about gate driver design or other circuit issues. GaN HEMTs are excellent transistors for the target voltage and current range, with the MASTERGAN1 rated to 600 [V], 10 [A], with a typical switching time less than 85 [nsec], perfectly adequate for 100 [V], 2 [A], 4 [MHz] maximum operation. Following the MASTERGAN1 circuitry, a boost converter provides an appropriate voltage for the switches from a 28 [V] nominal input, a typical aerospace power distribution potential. A flyback topology was chosen to boost the voltage because it can operate over a wide output range (designed for 50 - 100 [V]), is easily adjustable, and is appropriate for the power range of less than 200 [W]. With a change in the transformer design, different input and output voltage and power ratings may be easily accommodated. The GaN HEMTs chop this boosted DC voltage into square waves to actuate the individual PZT actuators attached to the solar cell.

3.5 Technical Specifications

Tables 3.3 and 3.4 give the physical and electrical specifications of the rotated CURVES prototype, assuming that 10 solar cells can be controlled by a single drive circuit, and that the system can be run four times per year, in 30 second spurts. Characteristics of Epo-Tek 323LP epoxy can be found at [7] and PZT characteristics can be found at [8] and [9].

Table 3.3. Physical Characteristics

	Additional Mass	Volume per Cell	Volume with Controller
Per Unit	43.45 [g]	207.64 $[mm^3]$	73807.64 $[mm^3]$

Table 3.4. Estimated Electrical Characteristics

Max Voltage	Average Voltage (Active)	Power per Usage Cycle	Average Run Time
100 [V]	95.00 [V]	66.44 [W]	3.00 [sec]
Duty Cycle	Power Usage (Inactive)	Overall Power Budget	Peak Power Usage
3.81×10^{-5} [%]	0.10 [W]	0.108 [W]	66.44 [W]

3.6 Design Changes

3.6.1 Surface Modification

Surface characteristics greatly affect the tendency of dust to adhere to a given object, as does electrical charge, especially when dealing with lunar regolith, which generally carries excess negative charge. Surface modifications can aid in dust mitigations by reducing the Van der Waals forces, reducing required actuation power or vastly increasing efficacy. Ultimately, the primary focus of the project was devoted to the function and optimization of the PZT actuators. However, experiments with Indium Tin Oxide (ITO) coated tempered glass, to compare the adherence of lunar simulant to glass, show promise as an avenue for future research and addition to CURVES.

Square samples of modified substances were adhered to a glass slide, had dust applied to them by aerosolization, (See Section 4.2.2) and vibrated ultrasonically at a twelve degree angle from the horizontal to remove dust. The amount of remaining dust was then compared visually and under a microscope.

3.6.2 Electrostatic Dust Shielding

Early in the project the team considered integrating an Electromagnetic Dust Shield (EDS) system with the CURVES PZT system for additional effectiveness. Several experiments test the efficiency of dust removal produced some promise, but ultimately proved too ineffective at removing fine dust particles, and the additional research was determined to be beyond the scope of the project.

3.7 Safety Plan and Protocols

For safe laboratory operations, all participants in the project underwent Missouri S&T General Lab Safety Training, broadly covering safety concerns that may arise during work on CURVES project. The hazards most commonly encountered were high-voltage and current circuits, and air-borne dust from the aerosolization process (Section 4.2.2) and aerosols. Risks from electric shock were largely mitigated by safe practices of making sure a circuit was dead before working with it and ample communication between team members. Air-borne hazards were mitigated by containing them as much as possible, as well as wearing dust masks while in use. Other safety protocols taken include common lab operation measures, such as the use of close-toed shoes while working with equipment, non-conductive clothing when working with circuits, including gloves, and other PPE and procedures as required.

4 Verification testing on Earth

4.1 Prototype Manufacturing

The team produced several glass slide-based prototypes using Epo-Tek 323LP epoxy and PZT-4 pieces of various dimensions. Difficulties arose relating to the tendency of the epoxy to flow out of the joint, especially in response to over-abundant application of the epoxy, and adhere the prototype to the fixture used to maintain the PZT position.

The manufacturing of the prototypes themselves required a method to place the PZT elements precisely and consistently. A precision-machined aluminum set block satisfied these constraints, with the added benefit of being modifiable for other designs by machining out new slots in the side designed to hold the PZT elements (Figure 4.1b).

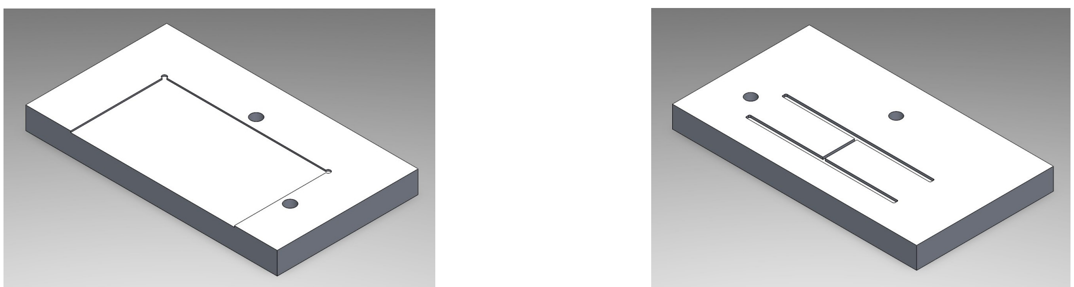

(a) Block Designed to hold Solar Cell

(b) Block Designed to Hold PZT in the Horizontal Configuration

Figure 4.1. CAD Models of the Horizontal PZT Set Block Design

Kapton tape prevented epoxy leakage affixing to the setting block. The block itself held a solar cell in one half (Figure 4.1a), and PZT elements, with epoxy applied to them, on the other (Figure 4.1b) with alignment dowels maintaining position throughout curing. Machining out the back of each block reduced the total heat capacity of the block, allowing sufficient heat to reach the bond to complete curing. Wire leads were soldered onto the exposed side of the actuators, as well as a ground lead to the metal substrate of the solar cell.

4.1.1 Bonding

Space-grade epoxy adheres the ceramic actuators that form the basis of CURVES to the solar cells they are intended to clean. A weak bondline carries the obvious danger of falling apart, and thick bondlines interfere with the effective transfer of vibrations from the actuators to the solar cells, making the strength and thickness of the bond line vital to the project. Early in the project, various methods of adhering the actuators were proposed, including metal sputtering, low-temperature co-fired ceramic (LTCC) nanofoil welding, and epoxies. All carried difficulties, mostly temperature related. The PZT actuators cannot be heated above 300 [°C] for any period of time without losing their polarization, requiring difficult re-polarization.

Two epoxies were evaluated on recommendations from the manufacturer, Epo-Tek, and the expertise of Dr. Yezad Anklesaria: Epo-Tek's 323LP and 353-ND formulations. The primary goal of the study was to determine which of these epoxies to utilize, whether or not to lode them to 15 $unitPERCENT$ silver to improve electrical conductivity, and the amount of pressure necessary to produce a desired bondline thickness of less than 10 [μm]. The study concluded that adding silver particles caused far too thick of bondlines, and a good bond line required curing pressures in excess of 500 [Pa].

Both epoxy formulations considered are two-part and are best cured by a step-cure method [10], curing in an oven at the recommended curing temperature for an hour, then allowed to cool with the oven. The samples were removed once the oven cooled, and any weights and alignment pieces were carefully removed. Step curing gives longer overall cure times, reducing trapped gasses, and ensuring more complete chemical reactions.

4.2 Concept Testing

Prior to prototype construction, ANSYS simulations determined optimal dimensions, arrangement, and orientation of PZT elements on solar cell prototypes. Determining the accuracy of these results proved necessary to verify that this sort of simulation is useful and effective in designing this system. Besides verifying simulation results, testing must be performed to show the system can be functional in lunar environments, especially in cryogenic vacuum conditions.

4.2.1 Benchtop Circuit

Test samples were driven by a large benchtop circuit during development of prototypes and a practical drive circuit as seen in Figure 4.2. This testing circuit consisted of a Tektronix AFG3022C Arbitrary Function Generator, used to control the frequency and voltage of the system. This fed through an E&I RF power amplifier to a pair of hot and ground alligator clips attached to the leads previously soldered onto the PZT actuator(s). On the ground cable running back to the amplifier, a Textronix TCP0030A current probe read the current back to a Tektronix MDO3014 Mixed Domain Oscilliscope so as to compare the frequency of voltage across the prototype–as measured by a Tetronix TPP0250 Voltage Probe connected to the hot and ground leads of the prototype–and current from the PZT sample.

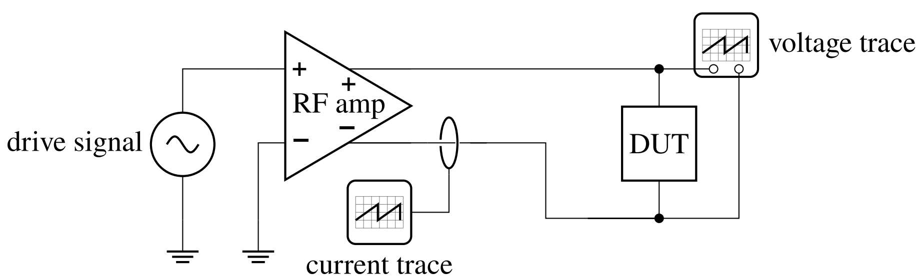

Figure 4.2. Benchtop Circuit

ANSYS simulation and analysis on a Hewlett-Packard 4294A Precision Impedance Analyzer gave estimates of true resonant frequencies to drive at. An impedance trace was run on the machine, which the sample is wired into via the soldered traces. At various points along the trace, sharp dips–immediately followed by sharp spikes–appear. By isolating and measuring these dips (which are at resonate frequencies) and spikes (known as anti-modes) the inductance-resistance-capacitance parameters of the Butterworth-van Dyke equivalent circuit model can be calculated for that particular frequency, used to determine the quality of the mode [11]. Refer to Section 4.3.2.1 for a discussion of the high power impedance measurement.

4.2.2 Dust Distribution Methods

A dust distributor was created to make a realistic, consistent, and uniform coating based on that used by Dr. Christopher J. Wohl's team at NASA's Langley Research Center [12, 13]. These distributors use compressed air to aerosolize simulant in order to spread it more evenly across the surfaces of samples, with particle size distributions more akin to those likely to be lofted onto lunar vertical solar panel arrays.

4.3 Prototype Testing Procedure

The efficacy of the dust removal relies on the accuracy of driving at the optimized resonance frequency, which is approximated by a characterization of each prototype after production. The resonance frequency of interest can shift across operating life and even a single cycle due to PZT aging and changes in mass to they system (i.e. addition and removal of dust). Frequency shifting of 5.5 [%] was recorded after testing. Typically the resonance frequency shifted downward. In testing, the 5.5 [%] frequency shift caused a reduced prototype efficacy of 50.6 [%], measured by SLDV surface motion. This makes driving the prototype at resonance and tracking changes in resonant frequency paramount to maximizing efficiency.

4.3.1 Testing Figure of Merit

This was To remove any dependence on testing changes on the results a normalizing factor was introduced for comparable results across prototypes and at different powers [14]. Deriving this normalizing factor starts with Newton's second law to develop a relationship between acceleration and the voltage induced by the piezoelectric transducers:

$$F = ma \tag{4.3.1}$$

The surface charge generated by the force is given by:

$$Q = dF \tag{4.3.2}$$

where d is the piezoelectric charge coefficient of the PZT. Voltage is defined as:

$$V = \frac{Q}{C} = \frac{dF}{C} = \frac{dma}{C} \tag{4.3.3}$$

where C is the capacitance between the electrodes,

$$C = \frac{\varepsilon A}{t} \tag{4.3.4}$$

where ε is the permittivity coefficient of the PZT, A is the surface area of the PZT, and t is the thickness.

The design variables subject to change are the PZT dimensions and the applied voltage. The other parameters are considered constants to create the resulting relationship:

$$a \propto \frac{VA}{t} \tag{4.3.5}$$

where the right hand side of the proportion is also known as the electric flux.

4.3.2 Initial Frequency characterization

Frequency control is essential to the actuation efficiency and efficacy. Due to optimization simplifications and manufacturing error, the prototype ideal frequency can vary from that identified in the FEA model. Each prototype was characterized using a high power impedance measurement technique to identify the frequency: the minimum impedance point across a frequency sweep corresponds to the highest quality structural mode, the mode of interest. Resonant frequency shifts with varying power; therefore, characterizing the mode at the driving power provides the best initial resonant frequency value.

4.3.2.1 High Power Impedance Measurement

Impedance analyzers use a low power signal (typical measurements range between 0.5 [μW] to 10 [mW]), sometimes causing the modes to not be fully pronounced and giving inaccurate results for resonant frequency at higher driving powers. To more accurately characterize the mode, the prototype was characterized at the testing power. The method used to measure the impedance requires a differential voltage probe across the PZT, a current probe on the negative return from the PZT, a function generator, RF amplifier, and an oscilloscope (See Section 4.2.1). The signal from the function generator (for this study, a Tektronix AFG3022C arbitrary function generator was used) swept across the frequency range where the mode may be present over a time range of 10 [msec] at an amplitude that would produce the driving amplitude desired through the amplifier, while an oscilliscope records just over one period of the frequency sweep using five million data points. MATLAB analysis of the resulting voltage and current signals returns the resonant frequencies.

To calculate the magnitude of the impedance response, the magnitude of the signal's frequency response of the voltage and current signals was first calculated by performing a Fast Fourier Transform (FFT) on the data. Second, the magnitude FFT response of the voltage was divided by the magnitude FFT response of the current to achieve the impedance response. The minimum impedance point can then be located for the prototype. An example for the horizontal prototype is shown in Figure 4.3.

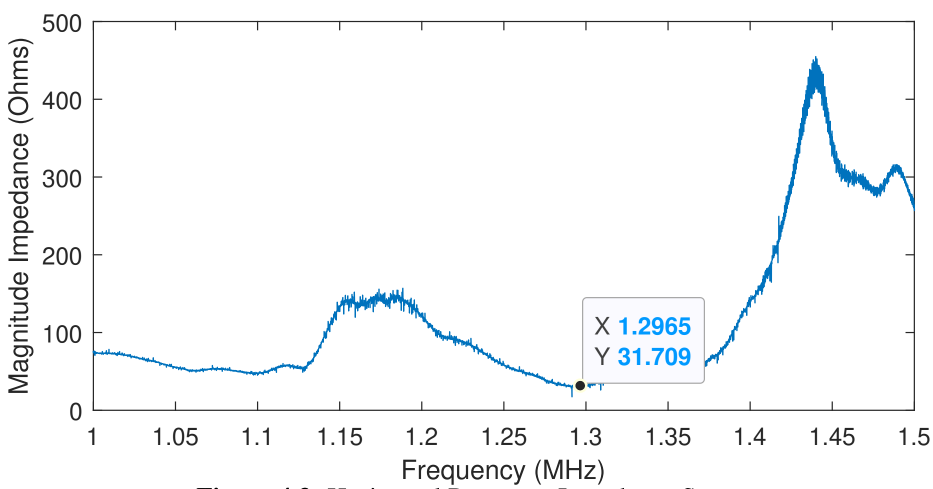

Figure 4.3. Horizontal Prototype Impedance Spectrum

4.3.3 ANSYS Verification

Testing in a laboratory atmospheric environment using an Optomet SWR Scanning Laser Doppler Vibrometer (SLDV) system evaluated overall prototype function and sought to verify ANSYS results for the prototype. Testing consisted of connecting each prototype to the bench top circuit discussed in Section 4.2.1 with the built-in signal generator on the SLDV providing the driving signal to the RF amplifier. Most tests were performed with a driving voltage of 30 [V] to prevent overheating of the prototype.

The SLDV characterized each prototype using approximately 4,000 points with a smart averaging of eight repetitions. Smart averaging removes poor data points, characterized as points with low coherence. The system also used dithering to improve measurement quality by slightly moving the measurement location. The metallic fingers printed on the solar cells presented the primary obstacle to accurate results. The SLDV measured the velocity normal to the scanner directly while the oscilliscope collects voltage and current data.

Analyzing the acquired velocity results in MATLAB calculated the average normal acceleration. First the average velocity magnitude over all of the points is calculated from the measured averaged FFT velocity magnitude data points from the SLDV. The velocity was then converted to acceleration at the frequency of excitation using the below equation:

$$a = 2\pi v f \tag{4.3.6}$$

where a is the acceleration, v is the velocity, and f is the frequency in hertz.

The acceleration was then normalized using the figure of merit outlined in Section 4.3.1.

4.3.4 I-V curve Testing

I-V curve tests were used to measure the prototype solar cell output at the following testing phases: 1) clean, before aerosolization, 2) lightly coated in dust after aerosolization, and 3) after prototype vibration testing, to measure the solar cell power reclaimed by PZT actuation.

A Python program in conjunction with a B&K Precision 8500 DC Electronic Load vie RS-232 interface produced I-V curves following the procedure outlined in [15]. The procedure consisted of measuring the open circuit voltage, V_{OC}, the most important I-V curve parameter dependent on the electronic load, at the lowest B&K 8500 operating voltage of 0.1 [V]. The program was written with "settle time" and "dwell time" parameters for each voltage step: settle time allowed time for transient load voltage step effects to become negligible. Dwell time was the time spent measuring at each voltage step, during which the voltage, current, power, and solar cell temperature were read continuously into the code and averaged.

A custom vacuum chuck , consisting of an aluminum block with alignment dowels and air channels for a vacuum pump to pull air underneath the solar cell during testing, kept the solar cell being tested securely placed and cooled it to prevent overheating. The setup is shown in Figure 4.4. A Source Four PARNel stage light, mounted above the vacuum chuck assembly at a distance of 33 [cm] from the stage light lens to the top of the vacuum chuck, provided lighting necessary for the solar cell to produce power.

The I-V curve tests also captured temperature data by thermocouples adhered to the back of each prototype, because the solar cell's output is inherently dependent on temperature (lower temperature cells produce higher power output) [16]. The procedure to measure an I-V curve consisted of starting both the stage light and the vacuum pump simultaneously, delaying 60 [sec], allowing the cell to reach a steady state temperature, then running the I-V curve Python program to capture I-V and temperature data. These I-V curve tests were replicated twice for the first characterization of a clean PZT to verify consistent results and once for for each test afterward. Representative I-V curve test results are shown in Figure 4.5.

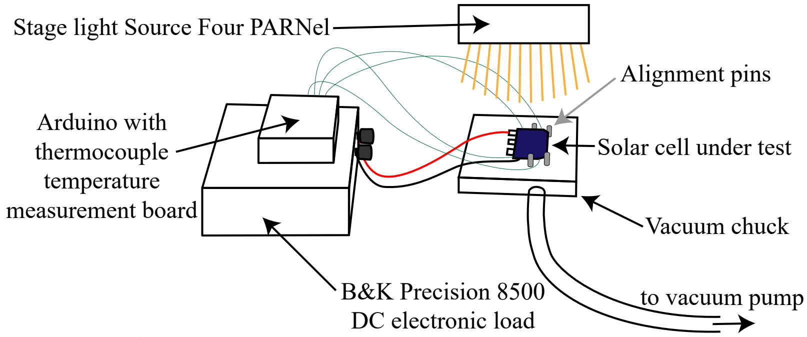

Figure 4.4. Illustration of the I-V Curve Testing Setup

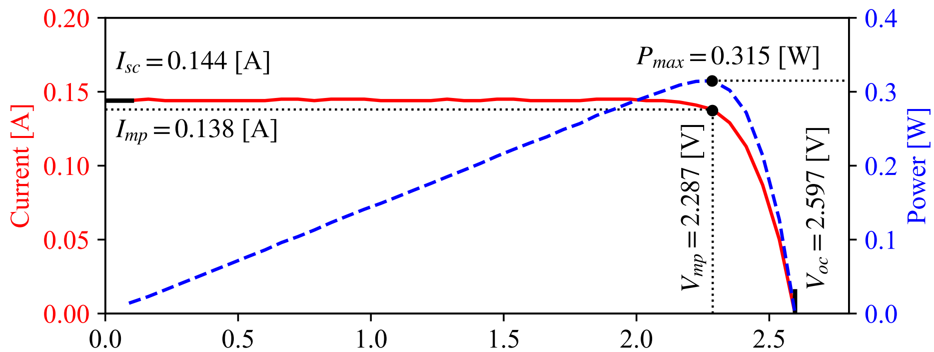

Figure 4.5. Clean Solar Cell, Rotated PZT Prototype I-V Curve

4.3.5 Cryogenic Testing

Cryogenic environment testing was carried out in a Janis liquid-helium cooled vacuum chamber. The prototype was brought to 168 [K] and 1.7×10^{-6} [Torr], then brought slowly back to laboratory conditions. Impedance measurements before and after cryogenic cycling verified that the prototype was capable of surviving cryogenic vacuum conditions. The actuation authority of piezoelectrics decreases with temperature [17], therefore the system can never be run while at cryogenic temperatures and need not survive actuation under cryogenic conditions.

4.4 Prototype Efficacy Testing

I-V curve testing compared the performance of the prototypes before and after actuation. Prototype testing occurred at various input voltages, measuring the voltage, current, and power input to the actuators, as well as the temperature of the prototypes. The system was also tested at three different angles, with the face of the solar cell horizontal, vertical, and ten degrees from the horizontal, simulating the tangential force from lunar gravity for a vertically oriented solar cell on the moon.

Each prototype is subject to testing at inputs ranging from 100 [mV] to 400 [mV], each test was observed with video, an oscilliscope capturing wave form, voltage, current, power, and a FLIR infrared camera to measure temperature. Thermocouples adhered to the back (inactive) side of each prototype measured temperature during I-V Testing.

5 Results and Conclusions

5.1 Prototype Testing Results

Figures 5.1 to 5.3 show the normal surface acceleration on the top of the solar cell, measured by the SLDV. The maximum acceleration occurred where the PZT elements were located. The ANSYS predicted normalized average acceleration underestimated the actual acceleration. The average power delivered to the prototypes and normalized accelerations are given in Tables 5.1 and 5.2. The ANSYS simulations under predicted the acceleration; the measured damping used matched the damping used in the ANSYS simulation. More work would need to be done to determine the cause of the underpredicted surface acceleration.

5.1.1 Solar Cell Power Reclamation

Table 5.3 shows the effect of dust on the solar cell. The square prototype's dust removal centered on the middle of prototype, while the horizontal and rotated prototypes removed dust more evenly. All prototypes improved in power generation efficiency after using the PZT actuators to clean the surface. The square prototype had an order of magnitude less maximum acceleration than the horizontal and rotated prototypes, but the acceleration was concentrated in the middle of the solar cell where the light was directed during the I-V curve tests, most likely causing the increased power performance of the square prototype.

5.1.2 Energy Reclaimed per Mass Cost by CURVES: Dust Mitigation Case Study

Consider the following projections for a lunar solar array. Let the integration problem be solved for the purposes of this case study, since it is primarily a matter of logistics. Let the circuit integration scale linearly up to the size of a solar array, and let the individual solar cell actuation require power on the scale of one test cycle (discussed in Section 4.4, see also Table 3.3).

Table 5.1. Average Power Delivered to the Prototypes

Prototype	Value	Magnitude	Phase [°]	Avg. Power [W]
Horizontal	Voltage [V]	85	242	70.7
	Current [A]	1.8	265	
Rotated	Voltage [V]	95	269	64.9
	Current [A]	1.9	313	
Square	Voltage [V]	174	210	18.2
	Current [A]	0.96	287	

Table 5.2. Measured Results

Prototype	Predicted Norm. Acc. $\left[\frac{1}{Vs^2}\right]$ x10^3	Measured Norm. Acc. $\left[\frac{1}{Vs^2}\right]$ x10^3	Percent Difference [%]
Square	59.0	61.232	3.66
Horizontal	373.4	1070.2	65.11
Rotated	244.8	3561.1	93.13

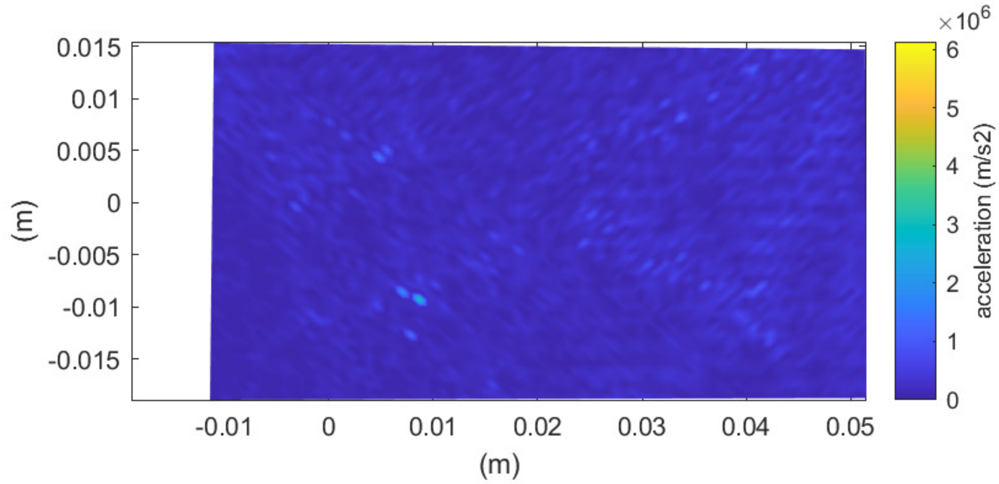

Figure 5.1. Horizontal Prototype Normal Acceleration Amplitude Measured

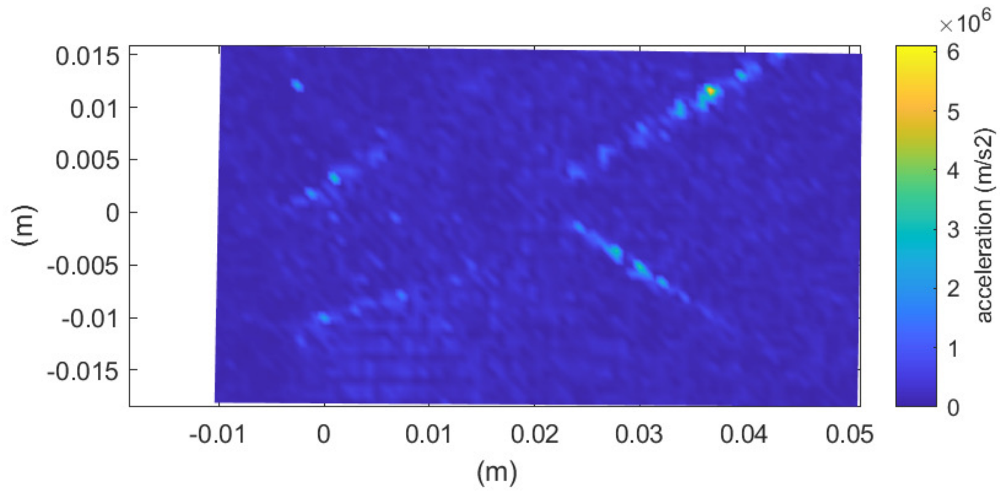

Figure 5.2. Rotated Prototype Normal Acceleration Amplitude Measured

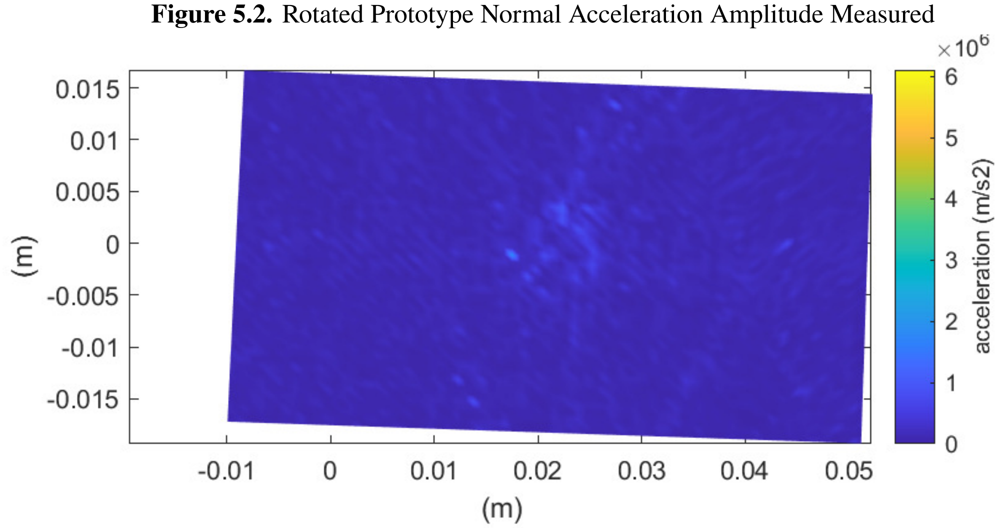

Figure 5.3. Square Prototype Normal Acceleration Amplitude Measured

Table 5.3. I-V Curve Power Results

Prototype	Angle	Initial Power [W]	Power with Dust [W]	Power after Cleaning [W]	Power Lost [mW]	Power Gained [mW]	Percent Regained [%]
Horizontal	Flat	0.335	0.314	0.319	21	5	23.8
	Moon Gravity	0.313	0.187	0.211	126	24	19.0
	Vertical	0.313	0.269	0.307	44	38	86.4
Rotated	Flat	0.321	0.298	0.313	23	15	65.2
	Moon Gravity	0.327	0.268	0.29	59	22	37.3
	Vertical	0.327	0.303	0.318	24	15	62.5
Square	Flat	0.322	0.306	0.311	16	5	31.3
	Moon Gravity	0.313	0.249	0.269	64	20	31.3
	Vertical	0.313	0.283	0.307	30	24	80.0

In a single three second cycle, CURVES shows the ability to reclaim 49 [%] of power lost to a light dust coating such as might be expected in environment. A 1-square-meter solar array, composed of 360 cells, requires an additional, 4.56 [kg] of control circuitry and actuators (See Table 3.3). This array is capable of generating an average of 115.32 [W] across its normal usage cycle when clean, but with a light coating of dust, this is reduced to 92.4 [W]. This gives an average power generation of 100.44 [W], showing CURVES capable of reclaiming 154 $\left[\frac{\text{MJ}}{\text{kg}}\right]$ of launch mass cost. Across one year, the energy per additional mass cost was 0.283 $\left[\frac{\text{MJ}}{\text{kg}}\right]$.

5.1.3 Cryogenic Testing

The square PZT prototype underwent thermal cycle testing according to the method introduced in Section 4.3.5. The prototype was brought to 168 [K] and 1.7×10^{-6} [Torr]. Impedance measurements before and after cryogenic cycling produced the results shown in Table 5.4, indicating no measured actuator degradation. Future high-temperature testing can similarly determine viability of CURVES in warmer environments.

Table 5.4. Impedance Before and After Cryostat Cycling of the Square PZT Prototype

Prototype		Mode		
		First [kHz]	Second [MHz]	Third [MHz]
Frequency	before	19.05	1.853	6.884
	after	19.05	1.853	6.880
Resonance quality factor, Q	before	20.0	13.8	194
	after	30.5	13.9	218
Q RMS error	before	6.2×10^{-4}	3.0×10^{-4}	1.7×10^{-2}
	after	6.6×10^{-4}	3.0×10^{-4}	1.6×10^{-2}

5.2 Circuit Testing

After verifying the controlling software using ModelSim, circuit testing was completed on the entire circuit. ModelSim allowed for isolated VHDL testing to ensure proper circuit function. Currently, the prototype circuit shows clear evidence of resonance tracking for resonant frequencies in the kilohertz range of frequencies. The prototype circuit struggles to identify resonant frequencies in the megahertz range, and instead tracks straight to the set minimum and maximum frequency boundaries. Tracking could be improved by cleaning up the output of the polarity detection circuit, Ipol. Keeping Ipol as clean and accurate as possible is imperative to the functionality of the PLL system, as this signal controls whether the PLL adjusts the operating frequency up or down.

The Arduino interface went through extensive tests and modifications, improving circuit testing efficiency and overall success. Manual operation tests revealed that the PZT would increase its temperature during actuation. As tests progressed, the program was updated to automate the signal output, allowing one to actuate the PZT in intervals to reduce these effects. Further tests revealed that the circuit worked best when bounds were selected closer to the nominal or resonant frequency. Thus the program can be automated to decrease the range of frequencies during PLL integration.

The control software supports up to four PZT elements. The software also supports varying the phase relationship, so that each of the four elements may be driven in-phase or out-of-phase, according to models that have been developed that identify the best operating conditions. The most recent test included two PZT specimens attached to a glass slide. After applying a light dust coating, the software actuated the two PZT elements simultaneously at various modes and phases. The results showed high efficacy at relatively low power and succeeded in moving even small particles. Further tests can include all four PZT as well as the flyback boost converter.

PLL testing showed equivalent dust mitigation capabilities with approximately 1.2 [W] of power, compared to driving at a constant nominal frequency and high power $\sim$ 60 [W].

5.3 Surface Modification Testing Results

Light layers of dust were scooped onto the surface being tested and vibrated via an ultrasonic cleaner. After testing, microscope images were analyzed to determine the efficacy of the surface modifications. Figure 5.4, makes clear that the grounded ITO coating was cleaned much more effectively than the glass substrate and the un-coated glass. Please refer to the additional verification demonstration file "Video4-SurfaceModificationTesting.mp4."

Numerically, at the same magnifications, the ITO glass, grounded had a remaining surface coverage of 0.06 [%] on average ranging plus or minus 0.05 [%]. All while the un-grounded ITO glass and Glass substrate respectively had 2.25 [%] and 2.45 [%] average coverage ranging plus or minus 2.6 [%]. All these

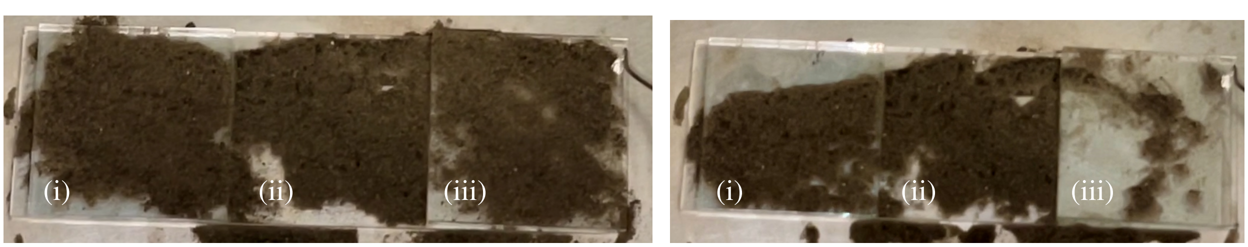

(a) Before Actuation **(b)** After Actuation

Figure 5.4. Ultrasonic Cleaning Results for Uncoated Glass (i), Glass Substrate (ii), and ITO Coated Glass (iii)

started at approximately a 30.38 [%] coverage on average.

Atomic force microscope (AFM) images of the surface morphology show the glass slide (Figure 5.5a), the ITO coated surface (Figure 5.5b), and a nano-imprinted polycarbonate surface (Figure 5.5c). The Z range for the ITO coated surface and nano-imprinted surface were 14.303 [nm] and 535.35 [nm] respectively, while the glass slide's Z range was 16.901 [nm]. From these tests, it can be seen that ITO surface coatings can improve the effectiveness of CURVES.

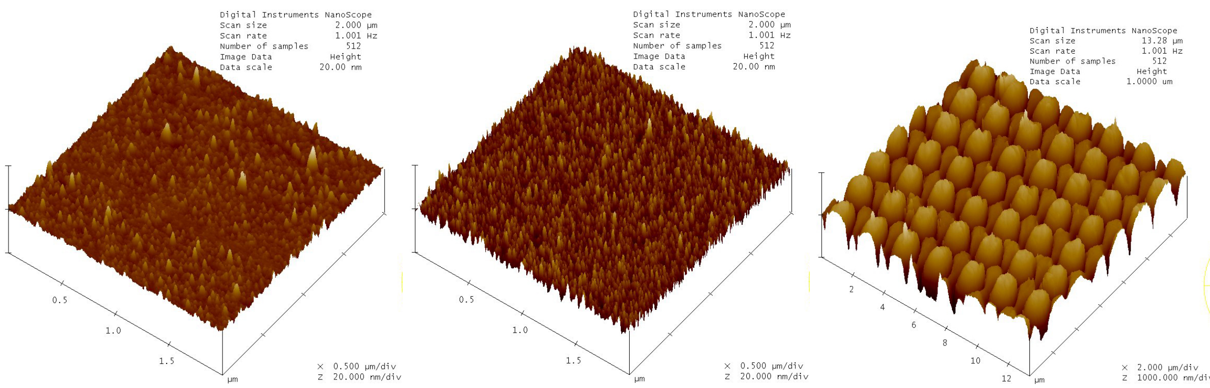

(a) Surface of Glass Slide

(b) Surface of ITO Coated Glass Slide

(c) Surface of Nano-Imprinted Polycarbonate Film on Glass Slide (Not to Scale)

Figure 5.5. AFM Images of Glass Surface and Coatings

5.4 Conclusions

All of the solar cell prototypes saw an increased power efficiency after lunar dust removal via piezoelectric excitation. From the testing, the PZT actuators achieved an average surface acceleration on the solar cell greater than predicted by finite element analysis. The acceleration produced was enough to break attractive adhesion forces between the lunar simulant and the solar cell. Additional testing in a vacuum can more accurately demonstrate the lunar simulants behavior in space environments. The assembled prototype was able to survive a cryogenic environment without losing the piezoelectric quality factor or destroying the bonding.

To aid in the dust removal process, surface coatings were tested to determine their effectiveness in dust removal. It was determined that the Indium Tin Oxide (ITO) coating helped reduce the static attraction forces between the lunar simulant and the solar cell surface. Additionally, a driving circuit for the prototypes was developed to make a compact package that could easily be added to existing solar arrays. The driving circuit also optimizes the prototypes efficiency by using a phase locked loop method to adjust the driving frequency to the optimal power point.

During testing in a laboratory environment, the solar cells were able to reclaim up to 86 [%] of the power lost due to the amassed lunar simulant, and the average power reclaimed was 49 [%]. The CURVES method combined with surface modification of solar cells offers a promising solution to the lunar dust challenge.

6 Path-To-Flight

Currently, the CURVES team has multiple functional solar-cell prototypes that have been tested to determine efficacy, durability, and efficiency. Additionally, a driving circuit has been designed and tested for function and impedance tracking.

Optimizing CURVES for space requires additional research, including durability testing and mass optimization. The PZT thickness was chosen to be one millimeter due to availability, but optimizing the thickness would lead to reduced mass and lower peak actuation stress. The circuit system also needs to be integrated into a final product package.

In addition, surface coatings have improved in the dust removal process. Initial testing with surface nano-imprinted polymer films (Figure 5.5c) worsened the dust removal process presumably due to increased electrostatic charge effects between the lunar dust and polymer surface. Testing with ITO coatings improved the dust removal process; ITO has a lower coefficient of friction and a higher hardness than glass, provides a conductive layer to minimize electrostatic forces, and is optically transparent. More work would need to be done to determine the best surface coating to aid CURVES in dust removal.

Another alternative approach to dust removal via piezoelectrics using surface acoustic waves (SAW) would need to be investigated. SAW waves offer the benefit of reduced stress in the substrate, reduced power cost, and reduced additional mass. Therefore, would be a possible alternative approach to exciting structural modes.

Before application to lunar and martian missions, CURVES requires further environment testing, especially in relevant heat and radiation environments. CURVES has been tested successfully in laboratory and cryogenic conditions.

Integration presents the greatest obstacle to creating a fully viable system ready for space flight. The design of solar cell arrays–especially how stiffly they are supported in a frame or mesh, and the hardness of the adhesives used to fix solar cells to the arrays–heavily influences the efficacy of CURVES. Additionally, the added mass and geometry requires collaboration with solar array designers to implement. Circuit integration is also closely tied to the design of solar arrays, as more wires must be run from a central controller to the various arrays, or alternately multiple controllers must be spaced across the arrays. Note, a new proposed solar array design is being developed [18], opening this integration problem to be solved by an integration design project.

Ultimately, CURVES is well-suited to operation on lunar rovers and other vehicles, providing dust mitigation with high durability and reliability, being nearly impervious to the effects of the dust itself, enabling CURVES to extend the mission life of vehicles, especially autonomous rovers, that otherwise might succumb to surface fouling and lose power generation.

7 Timeline

Table 7.1. Missouri University of Science and Technology NASA Big Idea Challenge Timeline

Task ID	CURVES: Contaminant Ultrasonic Removal via Vibration Ejection from Solar cells	February	March	April	May	June	July	August	September	October	November
1	***Bond layer***										
1.1	Literature review, company consultations	Masterbond			Epotek						
1.2	Bond thickness study						7/12/2021				
1.3	Bond decision						7/12/2021				
2	***Undergraduate teaching lectures***										
2.1	Piezoelectric crawler project	2/10/2021									
3	***Power research***										
3.1	Circuit prototype					PZT Test 7/7/2021					
3.2	Circuit review										
3.3	Power use case study									10/26/2021	
3.4	Circuit integration										
4	***Programming***										
4.1	Phase-lock loop										
4.2	VHDL					7/9/2021				10/17/2021	
4.3	Circuit integration									10/26/2021	
5	***ANSYS simulations***										
5.1	Non-optimized design characterizations				5/10/2021						
5.2	Multiphysics optimization script					6/15/2021					
5.3	Horizontal design optimization					6/28/2021					
5.4	Rotated design optimization							8/16/2021			
5.5	Electrical phase optimization								9/9/2021		
6	***Surface modification***										
6.1	ITO coating										
7	***Actuator design***										
7.1	Glass slide prototype tests										
7.2	PZT alignment jig design								9/14/2021		
8	***Testing***										
8.1	I-V curve program and thermal management				5/20/2021					10/13/2021	
8.2	Scanning laser doppler vibrometer (SLDV) testing						7/16/2021			10/18/2021	
8.3	Dusted testing				5/26/2021 Glass Slides						
8.4	Thermal cycling									10/25/2021	
8.5	Integrated circuit testing										
9	***Verification demo***										
9.1	Horizontal PZT prototype							8/9/2021			
9.2	Rotated PZT prototype								9/24/2021		
9.3	Horizontal PZT prototype II									10/9/2021	
9.4	Square PZT prototype									10/9/2021	
10	***Finalizing***										
10.1	Mid-project report				5/20/2020						
10.2	Technical paper									10/27/2021	
10.3	Presentation and poster										11/15/2021

8 Budget

Table 8.1. Missouri University of Science and Technology NASA BIG Idea Challenge Budget

(a) Phase I Expenditures

Revenue	
Grants-other organization-cash	82,879.63
Total Revenue	**82,879.63**
Expenses	
Graduate Student Assistants	14,597.64
Non-Academic Student Employees	23,316.48
Total Salaries & Wages	**37,914.12**
Grant Benefit Rate	0.00
Pay Based Benefits	0.00
FICA Benefits	1,052.94
Total Benefits	**1,052.94**
Lab supplies	1,193.69
Shop supplies	95.82
Laboratory - Non Capital	7,427.00
Vendor Discounts-Earned/Lost	-155.75
Laboratory - Capital	8,496.00
Laboratory - Capital (SLDV) Encumbered	137,250
Total Other Expenditures	**154,306.76**
Total Direct Costs	**193,273.82**
Indirect Costs-Grantor	4,832.46
Total F & A Costs	**5,228.06**
Total Expenses	**198,501.88**
Institutional Match	**115,622.25**
Excess of Revenues Over Expenditures	**0.00**
Ending Balance	**0.00**

(b) Phase II Expenditures

Revenue	
	33,390.16
Total Revenue	**33,390.16**
Expenses	
Tenure/Tenure-Track Faculty	22,141.31
Graduate Student Assistants	6,291.90
Non-Academic Student Employees	1,446.72
Total Salaries & Wages	**29,879.93**
Grant Benefit Rate	6,273.22
Pay Based Benefits	0.00
FICA Benefits	1,673.27
Total Benefits	**7,946.49**
Indirect Costs-Grantor	4,160.91
Total F & A Costs	**4,160.91**
Total Direct Costs	**37,826.42**
Total Expenses	**41,987.33**
Excess of Revenues Over Expenditures	**-8,597.17**
Ending Balance	**-8,597.17**

8.1 Significant External Sponsorship and Institutional Matching

S&T provided $115,622 towards the purchase of an Optomet scanning laser doppler vibrometer, and Optomet contributed by way of a $85,725 reduction in unit cost along with $57,000 (to date) in waiver of rental fees for temporary use of a demo unit until a custom-designed unit is delivered, for a total of $142,725.00.

A References

[1] L. Jaffe, D. Muhleman, C. Alley, R. Norton, S. Batterson, R. Scott, E. Christensen, E. Shoemaker, S. Dwornik, R. Steinbacher, et al., Principal scientific results from the surveyor program, Icarus 12 (2) (1970) 156–160.

[2] E. Slyuta, Physical and mechanical properties of the lunar soil (a review), Solar System Research 48 (5) (2014) 330–353.

[3] S. Kawai, Dust removal camera (US Patent no. 7,724,299, 2000).

[4] S. E. Cravens, Dynamic particle rejection on optical lenses using piezoelectric elements, Ph.D. thesis, University of Kansas (2011).

[5] S. A. Wagner, The apollo experience lessons learned for constellation lunar dust management, NASA Technical Publication TP-2006-213726. Washington, DC: National Aeronautics and Space Administration.

[6] NASA, Update on opportunity rover after martian dust storm (Oct 2018).
URL `mars.nasa.gov/news/8364/update-on-opportunity-rover-after-martian-dust-storm/`

[7] EPO-TEK 323LP Technical Data Sheet (Feb. 2021).
URL `https://www.epotek.com/docs/en/Datasheet/323LP.pdf`

[8] Energy harvester plate, Website (Oct. 2021).
URL `https://www.steminc.com/PZT/en/harvesting-plate-30x30x1mm-2-mhz`

[9] Ceramic materials, general characteristics.
URL `bostonpiezooptics.com/ceramic-materials-pzt`

[10] Epoxy Technologies, Cure Maters: Determining the Proper Cure Schedule.
URL `https://www.epotek.com/docs/en/Related/Cure Matters- Determining the Proper Cure Schedule.pdf`

[11] S. Butterworth, On electrically-maintained vibrations, in: Proceedings of the Physical Society of London, Vol. 27, IOP Publishing, 1914, pp. 410–424. `doi:10.1088/1478-7814/27/1/330`.

[12] C. J. Wohl, L. L. Foster, D. E. Connell, W. T. Kim, D. Yavas, A. Bastawros, J. W. Connell, Lunar dust simulant particle adhesion on copolyimide alkyl ethers, in: J. S. Levine (Ed.), The Impact of Lunar Dust on Human Exploration, Cambridge Scholars Publishing, 2021, Ch. 13, pp. 243 – 269.

[13] K. K. John, C. E. Rogers, Classifications and requirements for testing systems and hardware to be exposed to dust in planetary environments, Tech. rep., NASA (Sept 2021).

[14] K. Uchino, 5 - piezoelectric energy harvesting systems with metal oxides, in: Y. Wu (Ed.), Metal Oxides in Energy Technologies, Metal Oxides, Elsevier, 2018, pp. 91–126. `doi:https://doi.org/10.1016/B978-0-12-811167-3.00005-5`.

[15] K. Technologies, I-v curve characterization in high-power solar cells and modules, Keysight Technologies Application Note (2017) 1–11.

[16] E. Radziemska, The effect of temperature on the power drop in crystalline silicon solar cells, Renewable energy 28 (1) (2003) 1–12.

[17] X. Jiang, W. B. Cook, W. S. Hackenberger, Cryogenic piezoelectric actuators, in: Astronomical and Space Optical Systems, Vol. 7439, International Society for Optics and Photonics, 2009, p. 74390Z.

[18] Lunar Surface Innovation Consortium, May 27th Verical Solar Array Technology Confluence Meeting, Johns-Hopkins Applied Physics Laboratory, 2021.
URL `https://lsic-wiki.jhuapl.edu/display/SP/27 May 2021 - VSAT`

[19] M. K. Kurosawa, State-of-the-art surface acoustic wave linear motor and its future applications, Ultrasonics 38 (1) (2000) 15–19.

[20] A. Busnaina, G. Gale, Ultrasonic and megasonic particle removal, in: Precision Cleaning, 1995, pp. 347–359.

[21] R. A. Bowling, An analysis of particle adhesion on semiconductor surfaces, Journal of the Electrochemical Society 132 (1985) 2208–2214. `doi:10.1149/1.2114320`.

[22] A. Qi, J. R. Friend, L. Y. Yeo, Investigation of saw atomization, in: 2009 IEEE International Ultrasonics Symposium, 2009, pp. 787–790. `doi:10.1109/ULTSYM.2009.5441556`.

[23] H. Takizawa, S. Kawai, Camera and image pick-up device unit having an optical member that is vibrated to remove dust (US Patent No. 7,280,145, 2002).

[24] O. R. Walton, Adhesion of lunar dust, Tech. Rep. NASA/CR-2007-214685, NASA (2007).

[25] O. Walton, Review of adhesion fundamentals for micron scale particles, KONA Powder and Particle Journal 26 (2008) 129–135.

[26] J. Friend, D. Stutts, Dynamics of an annular piezoelectric motor stator, Journal of Sound and Vibration 204 (3) (1997) 421 – 437, piezoelectric motor stators;. `doi:10.1006/jsvi.1996.0944`.

[27] J. R. Friend, J. Satonobu, K. Nakamura, S. Ueha, D. Stutts, A single-element tuning fork piezoelectric linear actuator, Ultrasonics, Ferroelectrics and Frequency Control, IEEE Transactions on 50 (2) (2003) 179–186.

[28] J. R. Friend, D. S. Stutts, Design, optimization, and the prototyping of a small tuning-fork ultrasonic piezoelectric linear motor, in: IEEE Ultrasonics Symposium, Vol. 1, IEEE, Piscataway, NJ, United States, Caesars Tahoe, NV, USA, 1999, pp. 653–656.

[29] B. Research, Global automotive camera market to reach $14.19 billion by 2026, reports bis research (Jun 2018).
URL `https://www.prnewswire.com/news-releases/global-automotive-camera-market-to-reach-1419-billion-by-2026-reports-bis-research-685346581.html`

[30] R. Jones-Albertus, W. Cole, P. Denholm, D. Feldman, M. Woodhouse, R. Margolis, Solar on the rise: How cost declines and grid integration shape solar's growth potential in the united states, MRS Energy & Sustainability 5 (2018) E4. `doi:10.1557/mre.2018.4`.

[31] Department of Energy (DOE) Office of Energy Efficiency and Renewable Energy (EERE), Advanced Systems Integration for Solar Technologies: Solar Situational Awareness and Resilient Solutions for Critical Infrastructure, online (2018).
URL `https://eere-exchange.energy.gov/FileContent.aspx?FileID=e4a2ddcf-36c2-45cb-989e-9067e1a91c8b`

[32] International Society for Optics and Photonics, Transport powder and liquid samples by surface acoustic waves, Vol. 7291. `doi:10.1117/12.815387`.

[33] T. Saiki, A. Tsubosaka, A. Yamaguchi, M. Suzuki, Y. Utsumi, Interdigital transducer generated surface acoustic waves suitable for powder transport, Advanced Powder Technology 28 (2) (2017) 491 – 498. `doi:https://doi.org/10.1016/j.apt.2016.11.006`.

[34] F. O. Clark, R. Penny, J. Cline, W. Pereira, J. Kielkopf, Passive optical detection of a vibrating surface, SPIE Newsroom`doi:10.1117/2.1201407.005544`.

[35] J. C. Stover, Optical Scattering: Measurements and Analysis, Third Edition (SPIE Press Monograph PM224), SPIE Press, 2012.

[36] R. Blossey, Self-cleaning surfaces — virtual realities, Nature Materials 2 (5) (2003) 301–306. `doi:10.1038/nmat856`.

[37] K. A. F. Base, Xss-11 micro satellite (2011).
URL `https://www.kirtland.af.mil/Portals/52/documents/AFD-111103-035.pdf?ver=2016-06-28-110256-797`

[38] T. Davis, T. Baker, T. Belchak, W. Larsen, Xss-10 micro-satellite flight demonstration program, in: Proceedings of the AIAA/USU Conference on Small Satellites, Policies, Practices, or Methods to Enhance Low-Cost Space Access, SSC03-1-IV-1, 2004.

[39] K. A. F. Base, Automated navigation and guidance experiment for local space (2014).
URL `https://www.kirtland.af.mil/Portals/52/documents/AFD-111103-035.pdf?ver=2016-06-28-110256-797`

[40] S. Straight, C. Doolittle, T. Cooley, H. Gardner, P. Armstrong, R. Nadile, T. Davis, Tactical satellite-3 mission overview and initial lessons learned, in: Proceedings of the AIAA/USU Conference on Small Satellites, Policies, Practices, or Methods to Enhance Low-Cost Space Access, SSC03-1-IV-1, 2010.

[41] L.-H. Lee, Adhesion and cohesion mechanisms of lunar dust on the moon's surface, Journal of adhesion science and technology 9 (8) (1995) 1103–1124.

[42] G. Kumar, S. Smith, R. Jaiswal, S. Beaudoin, Scaling of van der waals and electrostatic adhesion interactions from the micro-to the nano-scale, Journal of adhesion science and technology 22 (5-6) (2008) 407–428.

[43] Y. Liu, L. A. Taylor, Characterization of lunar dust and a synopsis of available lunar simulants, Planetary and Space Science 59 (14) (2011) 1769–1783.

[44] L. A. Taylor, The role of lunar simulants versus apollo samples in isru activities, online (2010).
URL `nasa.gov/sites/default/files/atoms/files/taylor_apollo_vs_simulant.pdf`

[45] J. Rasera, J. Cilliers, J.-A. Lamamy, K. Hadler, The beneficiation of lunar regolith for space resource utilisation: A review, Planetary and Space Science (2020) 104879.

[46] T. Matsushima, T. Ishikawa, Particle grading effect on mechanical properties of lunar soil simulant fjs-1, in: Earth and Space 2014, Earth and Space, 2014, pp. 60–68.

[47] C. Schrader, D. Rickman, C. McLemore, J. Fikes, Lunar regolith simulant user's guide (2010).

[48] M. Jiang, Z.-Y. Yin, Z. Shen, Shear band formation in lunar regolith by discrete element analyses, Granular matter 18 (2) (2016) 32.

[49] K. Cannon, Planetary simulant database (November 2020).
URL `simulantdb.com/simulants/fjs.php`

[50] E. Robens, A. Bischoff, A. Schreiber, A. Dąbrowski, K. Unger, Investigation of surface properties of lunar regolith: Part i, Applied Surface Science 253 (13) (2007) 5709–5714.

[51] G. H. Heiken, D. T. Vaniman, B. M. French, Lunar Sourcebook, a user's guide to the Moon, Cambridge University Press, 1991.

[52] G. Arrhenius, S. Asunmaa, R. Fitzgerald, Electrostatic properties of lunar regolith, Lunar Science III, C. Watkins, ed.(The Lunar Science Institute, Houston, Tx.) 30.

[53] B. Jaffe, Piezoelectric ceramics, Vol. 3, Elsevier, 2012.

[54] M. J. Hyatt, Feighery, Lunar dust mitigation technology development, in: Lunar Dust Mitigation Technology Development, NASA, 2008.
URL `https://ntrs.nasa.gov/citations/20080047456`

[55] B.-H. Ryu, C.-C. Wang, I. Chang, Development and geotechnical engineering properties of kls-1 lunar simulant, Journal of Aerospace Engineering 31 (1) (2018) 04017083.

[56] C. M. Katzan, J. L. Edwards, Lunar dust transport and potential interactions with power system components, Tech. rep., National Aeronautics and Space Administration, Cleveland, OH (1991).

[57] J. R. Gaier, The effects of lunar dust on eva systems during the apollo missions, Tech. rep., NASA Glenn Research Center (2005).

[58] S. R. Singiresu, et al., Mechanical vibrations, 6th Edition, Pearson, London, UK, 2016.

[59] J. Rittenhouse, Y. Anklesaria, A. Koenig, D. S. Stutts, L. Tomanek, Z. Boeringa, Z. Reed, C. Thomasson, Contaminant ultrasonic removal via vibration ejection from solar cells (2020).

[60] A. W. Leissa, Vibration of plates, Vol. 160, Scientific and Technical Information Division, National Aeronautics and Space Administration, 1969.

[61] W. Soedel, Vibrations of shells and plates, Vol. 10, Marcel Dekker Incorporated, 1981.

[62] Z. Chai, Y. Liu, X. Lu, D. He, Reducing the adhesion and friction forces of si by coating ultra-thin al2o3 films, RSC Adv. 4 (2014) 51047–51054. `doi:10.1039/C4RA06379A`.

[63] G. A. Landis, Mars dust-removal technology, Journal of Propulsion and Power 14 (1) (1998) 126–128.

[64] Y. Ren, J. Tao, Z. Xue, Design of a large-scale piezoelectric transducer network layer and its reliability verification for space structures, Sensors 20 (15) (2020) 4344.

[65] V. Giurgiutiu, B. Lin, G. Santoni-Bottai, A. Cuc, Space application of piezoelectric wafer active sensors for structural health monitoring, Journal of Intelligent Material Systems and Structures 22 (12) (2011) 1359–1370.

[66] I. Ursu, D. Enciu, A. Toader, Towards structural health monitoring of space vehicles, Aircraft engineering and aerospace technology.

[67] C. M. Hartzell, D. J. Scheeres, The role of cohesive forces in particle launching on the moon and asteroids, Planetary and Space Science 59 (14) (2011) 1758–1768.

[68] R. Grieseler, T. Welker, J. Müller, P. Schaaf, Bonding of low temperature co-fired ceramics to copper and to ceramic blocks by reactive aluminum/nickel multilayers, physica status solidi (a) 209 (3) (2012) 512–518.

[69] X. Qiu, J. Wang, Bonding silicon wafers with reactive multilayer foils, Sensors and Actuators A: Physical 141 (2) (2008) 476–481.

[70] B. S. Yilbas, H. Al-Qahtani, A. Al-Sharafi, S. Bahattab, G. Hassan, N. Al-Aqeeli, M. Kassas, Environmental dust particles repelling from a hydrophobic surface under electrostatic influence, Scientific Reports 9 (1). `doi:10.1038/s41598-019-44992-9`.

[71] Epoxy Technologies, Using Mold Release Agents with Epoxy Adhesives.
URL `https://www.epotek.com/docs/en/Related/Tech Tip 22 Using Mold Release Agents with Epoxy Adhesives.pdf`

[72] Epoxy Technologies, Removing Bubbles from Epoxy.
URL `https://www.epotek.com/docs/en/Related/Tech Tip 4 Removing Bubbles from Epoxy.pdf`